CH$_4$-to-CH$_3$OH on Mononuclear Cu(II) Sites Supported on Al$_2$O$_3$: Structure of Active Sites from Electron Paramagnetic Resonance

Jordan Meyet, Anton Ashuiev, Gina Noh, Mark A. Newton, Daniel Klose, Keith Searles, Alexander P. van Bavel, Andrew D. Horton, Gunnar Jeschke, Jeroen A. van Bokhoven*, Christophe Copéret*

J. Meyet, A. Ashuiev, Dr. G. Noh, Dr. M. A. Newton, Dr. D. Klose, Dr. K. Searles, Prof. Dr. G. Jeschke, Prof. Dr. C. Copéret, Prof. Dr. J. A. van Bokhoven

Department of Chemistry and Applied Biosciences, ETH Zurich

Vladimir-Prelog-Weg 1-5, 8093 Zürich, Switzerland

E-mail: ccoperet@ethz.ch

Prof. Dr. J. A. van Bokhoven

Laboratory for Catalysis and Sustainable Chemistry, Paul Scherrer Institute Villigen 5232, Switzerland

E-mail: jeroen.vanbokhoven@chem.ethz.ch

Dr. A. P. van Bavel, Dr. A. D. Horton

Shell Global Solutions International B.V.

Grasweg 31, 1031 HW Amsterdam, The Netherlands

ABSTRACT: The selective conversion of methane to methanol remains one of the holy grails of chemistry, where Cu-exchanged zeolites have been shown to selectively convert methane to methanol under stepwise conditions. Over the years, several active sites have been proposed, ranging from mono-, di- to trimeric Cu(II). Herein, we report the formation of well-dispersed monomeric Cu(II) species supported on alumina using surface organometallic chemistry and their reactivity towards the selective and stepwise conversion of methane to methanol. Extensive studies using various transition alumina supports combined with spectroscopic characterization, in particular electron paramagnetic resonance (EPR), show that the active sites are associated with specific facets, which are typically found in γ- and η-alumina phase, and that their EPR signature can be attributed to species having a tri-coordinated [(Al$_2$O)Cu^{II}O(OH)]$^-$,T-shape geometry. Overall, the selective conversion of methane to methanol, a two-electron process, involve two of these isolated monomeric Cu(II) sites that play in concert.

Introduction

The direct and selective conversion of CH$_4$ to CH$_3$OH could transform the petrochemical industry, by enabling on-site conversion of CH$_4$ on a scale much smaller than is currently viable. Existing routes, which are both energy-

30   intensive and indirect, require the generation of syngas (H_2/CO) through CH_4 reforming that can then be converted

31   to CH_3OH. Cheap and abundant CH_4 is the main constituent of natural gas (70-90 %), but its transportation in liquid

32   form is energy demanding and comes at additional cost. Although the development of catalytic processes for the

33   partial oxidation of CH_4 is highly desirable, this reaction remains challenging due to the low reactivity of CH_4

34   compared to that of CH_3OH which leads to facile generation of over-oxidized and unwanted products (e.g. CO,

35   CO_2).[1–4] In nature, methane monooxygenases (MMOs, with either Fe or Cu active sites) are highly efficient at

36   performing this selective oxidation.[5] The particulate form of this enzyme (pMMO) possesses several copper-con-

37   taining sites for which the exact structure and nuclearity are still under debate.[6–8] Initial studies ascribed the active

38   site as a dimeric copper species present in the PmmoB subunit (Cu_B, Fig. 1a)[9]. A more recent report, supported by

39   electron paramagnetic resonance (EPR) spectroscopy has, however, shown the exclusive presence of mononuclear

40   sites in pMMO; the Cu_C site located in the PmmoC subunit has been assigned to the metal binding site responsible

41   for hydrocarbon binding and oxidation(Fig. 1a).[8]

42   In parallel, promising processes based on inorganic materials have been developed in recent years. These processes

43   rely on chemical looping, which decouples an aerobic (O_2) oxidation step from the CH_4 activation step, and there-

44   fore curtails over-oxidation of the methoxy species formed.[10,11] The most-studied materials within the chemical

45   looping paradigm are copper-exchanged zeolites. Different types of active centers have been proposed based on

46   spectroscopic characterization.[12] These proposals include a dinuclear mono-μ-oxo $[Cu–O–Cu]^{2+}$ center[13] (Fig. 1a)

47   and a trinuclear $[Cu_3O_3]^{2+}$ core.[14] In addition, monomeric Cu sites $[CuOH]^+$ in chabazite,[15] and two monomers pre-

48   sent in the 12-membered-ring channels of mordenite have been proposed based on density functional theory (DFT)

49   calculations.[16] However, despite major efforts, the active site structures remain highly debated. This deficit not-

50   withstanding, substantial improvements in CH_3OH yield per chemical looping cycle have been achieved to reach

51   the theoretical limit of CH_3OH for two Cu(II) sites.[17] However, state-of-the-art zeolite-based materials remain eco-

52   nomically unviable for commercial applications because of an insufficient amount of reactive sites per unit mass

53   and the long cycle times associated with this step-wise process.[18,19] Thus, alternate materials must be explored for

54   this challenging transformation. Copper supported on silica produces CH_3OH,[20–22] however the obtained yield is

55   low and the active sites are ill-defined (small CuO clusters). Recently, we showed that proximal monomeric Cu(II)

56   sites supported on alumina, and generated via the surface organometallic chemistry (SOMC) approach,[23] can con-

57   vert CH_4 to CH_3OH.[24] However, the mixed (Si/Al) surface environment arising from a preparation method that

58   employed a Cu(II) siloxide precursor, combined with the complexity of the alumina surface, rendered the unam-

59   biguous assignment of the reactive Cu(II) centers challenging. We thus reasoned that the formation of well-dis-

60   persed Cu(II) in a pure alumina environment, using a copper-aluminate molecular precursor, would enable the

61   identification of the active site structure (Fig. 1b).
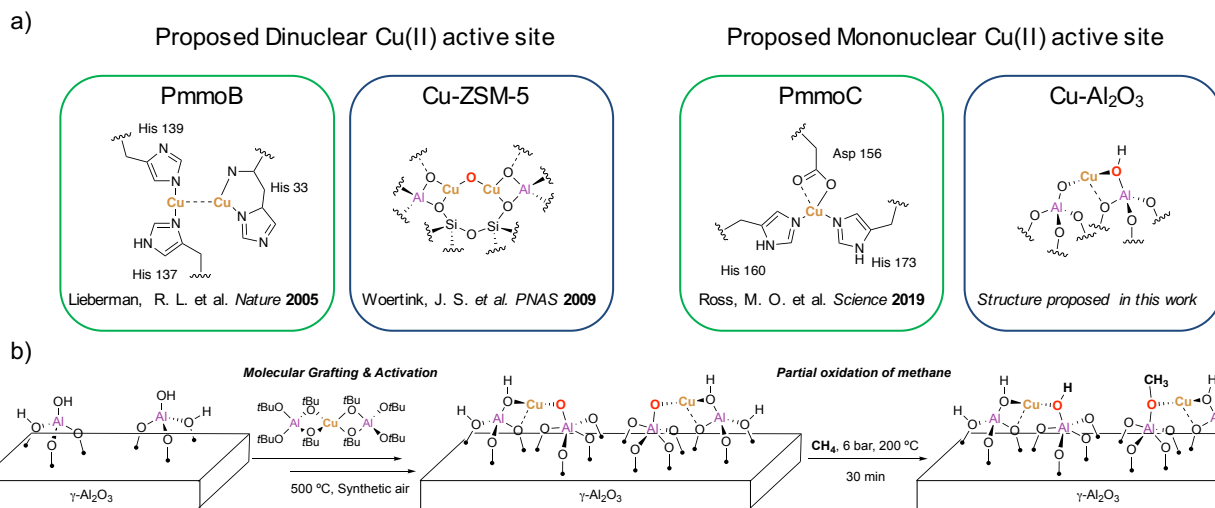
Figure 1. a) Proposed dinuclear (left) and mononuclear (right) active sites in the enzyme Pmmo (green frame) and the equivalent (in terms of copper nuclearity) analogs proposed for Cu supported on oxide supports (blue frame); **b)** Schematic illustration of the strategy used to generate monomeric Cu(II) sites in a pure alumina environment and the subsequent reaction with CH_4 to form hydroxy and methoxy species.

Here we report the formation and characterization of well-dispersed Cu(II) sites on partially dehydroxylated transitional alumina generated via SOMC followed by thermal activation. Characterization by *in situ* EPR spectroscopy allows for the spectroscopic identification of reactive Cu(II) surface sites involved in the selective partial oxidation of CH_4. These reactive sites display a unique EPR signature, which can be observed for Cu(II) on γ-, η- and θ-Al_2O_3 but not for non-defective α-Al_2O_3. Combining X-ray adsorption spectroscopy (XAS), advanced EPR methods and computational modeling enabled the assignment of the reactive monomeric Cu(II) sites on alumina as a tri-coordinated $[(Al_2O)CuO(OH)]^-$ species.

Results

Formation of Cu monomers on γ-alumina

The copper aluminate molecular precursor,[25] $[Cu(\kappa^2\text{-}Al(OtBu)_4)_2]$ (**1**) (see ESI Section 3, Figs. S1 - S5 for the full characterization of **1**) was grafted on γ-Al_2O_3 ("γ-a") dehydroxylated under vacuum at varied temperatures (denoted by X in degree Celsius in "γ-a$_X$"): **γ-a$_{500}$** (OH density, Θ = 2.4 OH.nm^{-2}), **γ-a$_{700}$** (Θ = 0.9 OH.nm^{-2}) and **γ-a$_{800}$** (Θ = 0.4 OH.nm^{-2}) (see also ESI Figs. S6 & S7), to yield the corresponding grafted materials **1-γ-a$_X$**. These grafted materials were characterized by UV-vis, diffuse reflectance infrared (DRIFTS), EPR and X-ray adsorption near-edge spectroscopies (XANES) (ESI Section 4 & Figs. S7 – S9). All **1-γ-a$_{X00}$** materials show similar spectroscopic features, indicating the generation of similar surface species after grafting irrespective of the initial dehydroxylation temperature for γ-Al_2O_3. The presence of Cu(II) was confirmed by both EPR and the observation in the electronic spectra of the d-d transition characteristic of Cu(II) species. However, the presence of a pre-edge feature at 8983 eV in the XANES, characteristic of Cu(I) species, indicates the partial reduction of the total Cu speciation (Fig. S9), as previously observed when different Cu(II) precursors were grafted on alumina.[24]

3

89 Thermal activation of these **1-γ-a$_X$** materials under a flow of dry synthetic air at 500 °C leads to the exclusive

90 generation of organic-free Cu(II) surface species (**1$_{500}$-γ-a$_X$**), as demonstrated by IR, UV-Vis, EPR and XANES

91 (Section 4, Figs. S10 – S12). Continuous wave (CW) X-band EPR analysis of the activated material (Fig. S12)

92 shows the presence of paramagnetic Cu(II) species in a nearly axial environment ($g_\parallel > g_\perp > g_e$) with well-resolved

93 Cu hyperfine coupling, which confirms the presence of monomeric Cu(II) species well-dispersed on the alumina

94 support.[24] Comparison of the CW EPR spectra amongst the activated Cu generated on the partially dehydroxylated

95 alumina at different temperatures (*vide infra*), allows the identification of at least two different Cu species based on

96 the observed parallel transitions ($A_\parallel$ and $g_\parallel$): $A_\parallel \approx 370$ MHz and $g_\parallel \approx 2.39$ for one site (denoted site I) and $A_\parallel \approx 440$

97 MHz and $g_\parallel \approx 2.33$ for the remainder of the signal (denoted site II, but which is composed of multiple species; *vide*

98 *infra*) (Fig. S12). The ratio between these two sites is highly dependent on the initial dehydroxylation temperature

99 of the alumina support prior to grafting. A dehydroxylation temperature of 500°C (**1$_{500}$-γ-a$_{500}$**) yields predominantly

100 site I, whereas dehydroxylation at 800°C (**1$_{500}$-γ-a$_{800}$**) gives primarily site II.

101

102 Reactivity of the material

103 The activated materials, **1$_{500}$-γ-a$_X$**, were reacted under 6 bars of CH$_4$ at 200°C for 30 min and isolated under inert

104 conditions for further spectroscopic characterization. DRIFTS analysis after reaction shows the appearance of two

105 bands at 2957 and 2853 cm^{-1} assigned to the asymmetric and symmetric stretch of methoxy surface species, respec-

106 tively (Fig. S13).[26] This assignment was confirmed by ^{13}C solid-state nuclear magnetic resonance (SSNMR) of **1$_{500}$-**

107 **γ-a$_{500}$** reacted with ^{13}CH$_4$, where two distinct peaks are observed in the ^{13}C NMR spectra: a major broad peak at 48.3

108 ppm along with a minor peak at 64 ppm, assigned respectively to surface methoxy/methanol (CH$_3$O(H)–) and small

109 amounts of dimethyl ether (DME) (Fig. S14).[27] After extraction with water at 120 °C, the **1$_{500}$-γ-a$_{500}$** material shows

110 the highest CH$_3$OH productivity among all samples with 0.12 mol CH$_3$OH/mol of Cu. The CH$_3$OH yields for the

111 other materials are lower, with **1$_{500}$-γ-a$_{800}$** yielding only half the amount of CH$_3$OH (0.06 mol CH$_3$OH/mol of Cu;

112 ESI Table 1). To understand the origin of the observed reactivity, the reaction with CH$_4$ was monitored by *in situ*

113 EPR spectroscopy (Fig. 2a). For all materials, the initial spectra include a mixture of sites, while after reaction only

114 the signal associated with site I completely disappears, leaving a broad signal consisting of a distribution of unre-

115 active Cu monomers described as site II (Figs. 2a, S15–S16). The partial disappearance of the EPR signal can be

116 rationalized by the reduction of reactive Cu(II) species to EPR-silent Cu(I). Furthermore spin quantification, ob-

117 tained from double integrals of the signal before and after reaction, is consistent with the expected number of

118 electrons (2 e$^-$ for CH$_4$ to CH$_3$OH) required for the selective reaction with CH$_4$ (Fig. 3a).[24] This Cu(II)/Cu(I) redox

119 process is further evidenced by Cu K-edge XANES analysis of material **1$_{500}$-γ-a$_{500}$** before and after reaction, which

120 shows the emergence of a Cu(I) pre-edge feature (Fig. S17) similar to previous reports for zeolitic-[28] and alumina-

121 based systems.[24] Thus, the EPR signal of the reactive Cu(II) species can be obtained by subtracting the spectra

122 between the reacted and unreacted materials, revealing the spectroscopic signature of the reactive monomeric Cu(II)

123 site (site I). In contrast to many spectroscopic techniques, which characterize both reactive and spectator Cu(II)

124 sites, this EPR signature belongs exclusively to the reactive centers involved in the redox reaction.
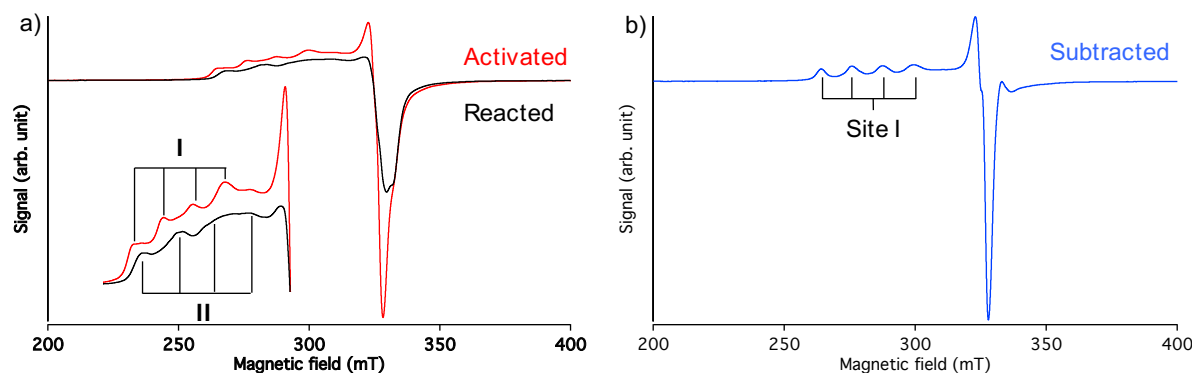
Figure 2. a) *In situ* X-band EPR spectra (298 K) for 1_{500}-γ-a_{500} before and after reaction under 6 bar of CH_4 for 30 min at 200 ºC **b)** X-band EPR difference spectrum (298 K) before-after reaction

The maximum ratio of reduced Cu(II), determined from the double integrals of the signals before and after reaction, was observed for 1_{500}-γ-a_{500} with 31 % of Cu(I) formed for a CH_3OH yield of 0.12 mol CH_3OH/mol of Cu (Fig. 3a). Cu K-edge EXAFS analysis of 1_{500}-γ-a_{500} by (Fig. S18, Table S2) indicates an average of 3 O in the first coordination sphere of the Cu center and, crucially, the absence of a Cu-Cu path consistent with the presence of Cu monomers. Comparing the first shell between the initial and reacted states does not reveal significant changes in the local Cu–O coordination sphere (Fig. S18, Table S2). The interpretation of the EXAFS is, however, limited by a relatively reduced dataset and low signal-to-noise ratio. Moreover, EXAFS averages over all (both active and inactive) Cu species present; and, in these cases these different contributions cannot be disentangled with any degree of precision or specificity.

By contrast, EPR spectroscopy permits more selective probing of the reactive site (*vide supra*). Taking advantage of the specificity of this spectroscopy, a wider range of transitional alumina supports was explored (η-, θ- and α-Al_2O_3) to better understand the formation and identity of this reactive monomeric Cu species. Transition aluminas provide different anchoring sites on the support by exposing different low-index planes and facets, although the nature of specific facets remains a matter of debate. The γ- and η-Al_2O_3 phases are of particular interest because of their high Lewis acidity and similar reactivity.[29] In fact, both are able to coordinate N_2 with a blue shifted IR band at 2355 cm^{-1}, assigned to adsorption at tri-coordinated Al (Al_{III}) for γ-Al_2O_3.[30] Such highly Lewis acidic undercoordinated sites are absent on α-Al_2O_3 surface.

Similar grafting and activation procedures were applied for these different transition aluminas, leading to the generation of well-dispersed Cu(II) species (Figs. S19 – S24) supported on Al_2O_3, 1_{500}-z-a_X (where "z" denotes the phase of the transition alumina employed). Post reaction with CH_4, the surface speciation for each of these materials, was again probed using DRIFTS (Fig. S25). Material reactivity was assessed by *in situ* EPR spectroscopy, coupled with CH_3OH quantification (Figs. S26 – S30, Table S3). In all cases, except for 1_{500}-α-a_{500}, only sites I and II were observed in EPR spectra of the activated material (Figs. S26-S29). Upon reaction with CH_4, only site I disappeared. For 1_{500}-α-a_{500}, CH_3OH could not be quantified, and the low intensity EPR signal observed for Cu(II) (Fig. S30), likely due to the very low specific surface area (3 m^2.g^{-1}) and the small amounts of supported Cu, is unperturbed by

5

154 reaction with CH_4. The CH_3OH yield measured for all other materials, however, correlates with the disappearance

155 of EPR signal (Fig. 3a) as was previously observed in the case of 1_{500}-γ-a_X.
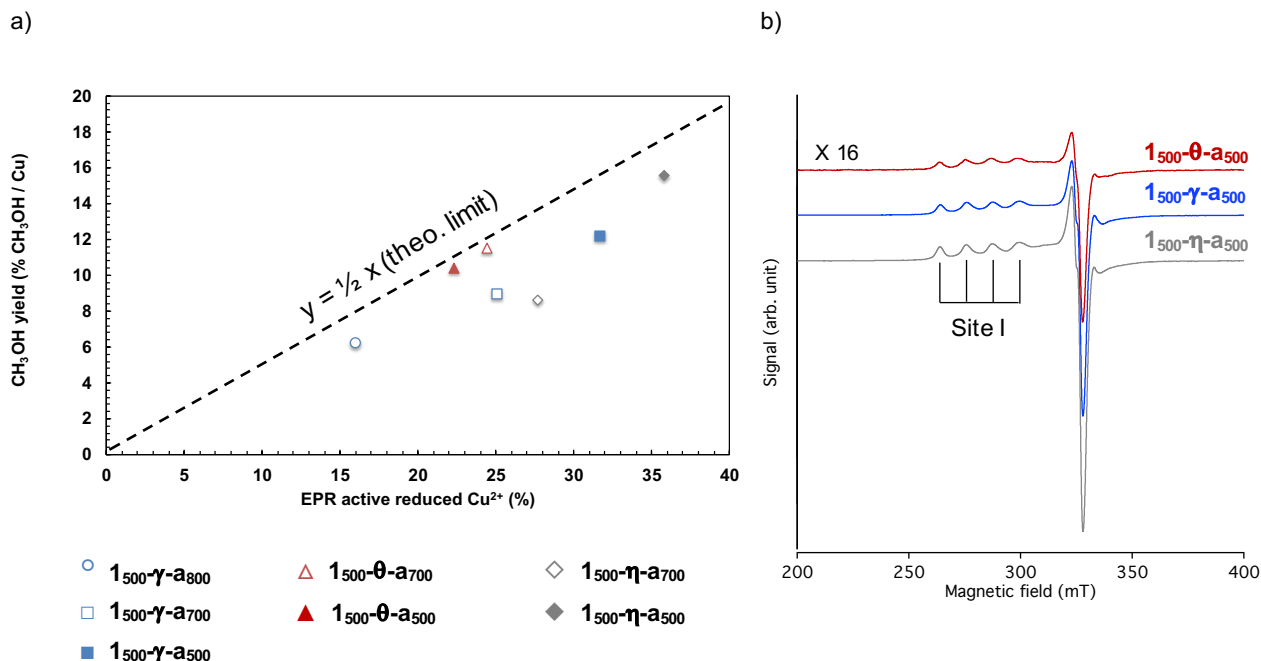
156

157 **Figure 3. a)** Reducibility of the monomeric Cu site determined by double integration of EPR *in situ* reaction (in %
158 of Cu) versus CH_3OH yield obtained after reaction with CH_4 in mol CH_3OH/mol of Cu, for the different Cu sup-
159 ported transitional aluminas tested. Deviation from the theoretical limit (dash line), indicating the 2 electrons re-
160 quired for the formation of CH_3OH, provides information on the material selectivity toward CH_3OH, and **b)** X-
161 band difference EPR spectra (298 K) before-after reaction of 1_{500}-a_{500} supported on various transitional alumina
162 displaying identical reactive Cu(II) monomeric site I.

163

164 Greater reactivity is observed for 1_{500}-η-a_{500} (0.16 mol CH_3OH/mol Cu), compared to that for 1_{500}-γ-a_{500} (0.12 mol

165 CH_3OH/mol Cu), which could be rationalize by higher Lewis acidity for η-a_{500} compared to γ-a_{500}, and the presence

166 of greater amounts of defective undercoordinated aluminum (Al_{III}) surface sites. These Al_{III}, and their relative

167 amounts, are evidenced by the area of the band of coordinated N_2 observed in the IR spectra of the dehydroxylated

168 Al_2O_3 (Fig. S19). This enhanced reactivity suggests that Cu sites are located in close proximity to surface Al_{III}

169 defective sites.[31–33]

170 Low-temperature CW EPR, and simulation of the EPR parameters, was performed for 1_{500}-η-a_{500}, which possesses

171 the highest fraction of reactive site I. The EPR spectra of the activated and reacted material for 1_{500}-η-a_{500} (Fig. 4a)

172 are similar to those observed for 1_{500}-γ-a_{500}. The resulting difference spectra, corresponding to the reactive, nearly

173 axial, monomeric Cu(II) species observed on all the materials studied, can be simulated with the *g* tensor parameters

174 *g* (site I) = [2.0625 2.0787 2.3923], and hyperfine coupling A_{Cu} (MHz) = [30 38 400] (Fig. 4b), while the inactive

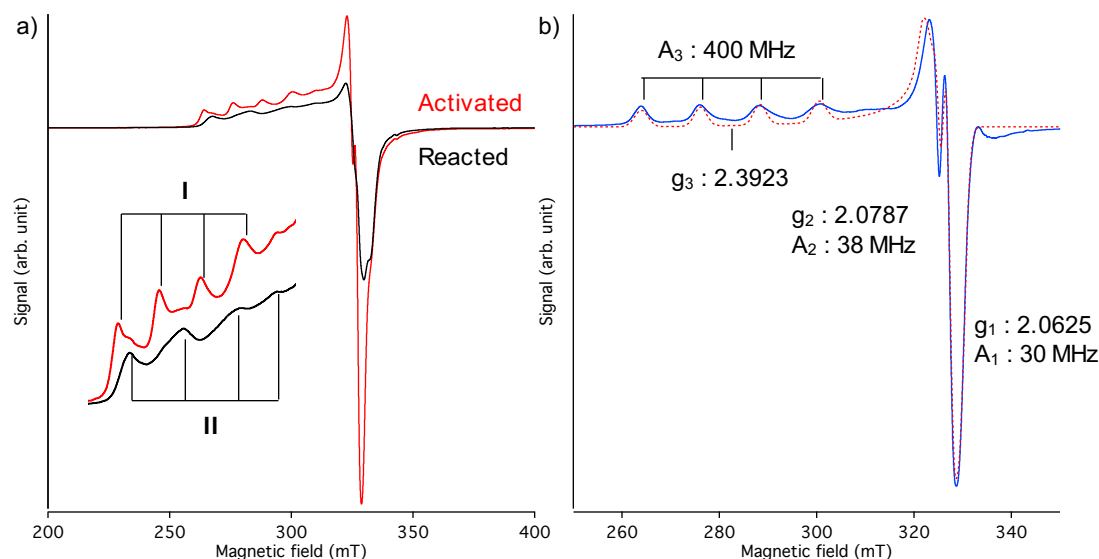175 sites (site II) correspond to a mixture of at least two distinct species (ESI Fig. S31).

Figure 4. a) X-Band EPR spectrum (103 K) for 1_{500}-η-a_{500} before and after reaction under 6 bar of CH_4 for 30 min at 200 °C, and **b)** X-band EPR difference spectrum (103 K) for 1_{500}-η-a_{500} before-after reaction (plain) and the resulting simulation (dashed) parametrizing the spectrum of the active species.

To further characterize the reactive species, 1_{500}-γ-a_{500} was contacted with CO as a probe molecule and monitored by IR and EPR (Figs. S32 & S33). After introduction of 110 mbar of CO, followed by evacuation, new features are observed by IR in the range of 1700 – 1200 cm^{-1}. The difference between the reacted and activated spectra reveal the appearance of bands at 3611 cm^{-1} (ν_{OH}), 1647 cm^{-1} ($\nu_{s\,OCO}$), 1479 cm^{-1} ($\nu_{s\,OCO}$), 1443 cm^{-1} ($\nu_{s\,OCO}$), 1233 cm^{-1} (δ_{OH}) (Fig. 5a & Fig. S32). These bands are associated with stable bicarbonate ($HOCO_2^-$) surface intermediates formed during the oxidation of CO, as previously reported for the interaction of CO_2 with γ-Al_2O_3.[34] The same experiment monitored by EPR spectroscopy results in partial disappearance of site I along with appearance of a new EPR signal (Fig. 5b & Fig. S33). Difference spectra confirm the involvement of the reactive monomeric Cu(II) site for the one-electron oxidation of CO to a $HOCO_2^{-\bullet}$ radical anion. Similar reactivity was observed for 1_{500}-η-$Al_2O_{3\text{-}500}$ under identical conditions (Fig. S34). The new signal, which has an effective g value of 2.0026, possesses an effective super-hyperfine coupling of 50 MHz, as determined from simulation (Fig. 5c). The presence of 11 lines for the radical species formed can be explained by hyperfine interaction between the radical center with two equivalent Al nuclei ($A_{eff}(^{27}Al)$ = 50 MHz). Similar super-hyperfine couplings were observed by Gafurov *et al*. upon contacting γ-Al_2O_3 with anthraquinone, which were associated to a tetra-coordinated Al_{IV} pair.[35] This experiment with CO further supports the assignment of a unique reactive monomeric Cu(II) species (site I) for the selective conversion of CH_4 to CH_3OH. From the reactivity observed during the one-electron oxidation of carbon monoxide, one can probe the chemical surrounding of the active center. The formation of a bicarbonate radical along with the observed hyperfine coupling constant is consistent with the presence of a hydroxyl group and two equivalent Al_{IV} in the coordination sphere of the reactive Cu(II) center.
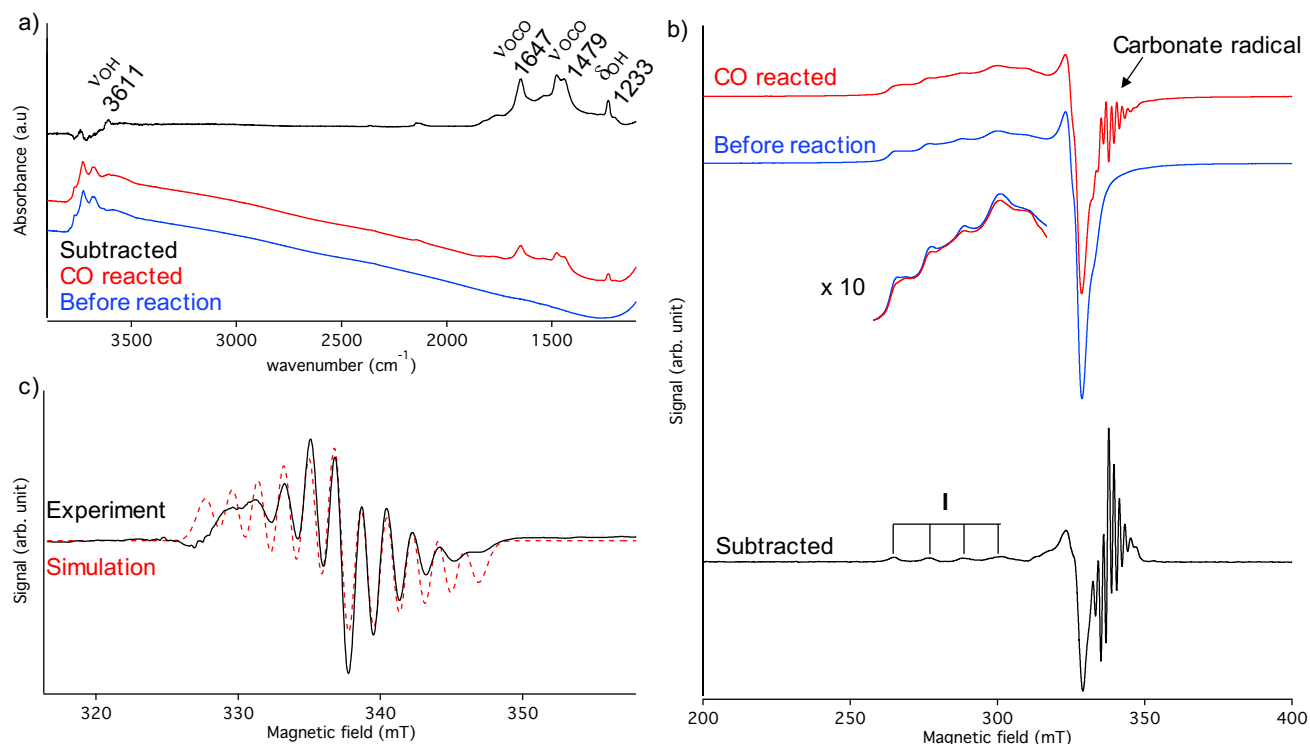
Figure 5. a) FTIR and **b)** X-band EPR spectra (298 K) of $\mathbf{1_{500}}$-γ-$\mathbf{a_{500}}$ before (blue) and after (red) reaction with 110 mbar of CO at room temperature and the corresponding difference spectrum (black). **c)** Extracted EPR signal of the carbonate radical formed upon reaction with CO (black) and simulation (dashed red) [g_{eff} = 2.0026 and A_{eff} = 50 MHz].

We further investigated the reactive species (site I) in $\mathbf{1_{500}}$-η-$\mathbf{a_{500}}$, which contains the highest amount of reactive Cu(II), with hyperfine sublevel correlation spectroscopy (HYSCORE)[36]. Note that the inactive species (site II) are in fact silent in X-band HYSCORE spectra (see Fig. S36) such that this method allows for selective observation of the ^{1}H and ^{27}Al couplings of the reactive species. The HYSCORE spectrum of the reactive species, measured at the magnetic field position corresponding to the maximum intensity of the echo-detected EPR spectrum (Fig. 6a), reveals the presence of coupled ^{1}H nuclei in close proximity to the Cu(II) center, together with a distribution of ^{27}Al couplings (Fig. 6b). The HYSCORE spectrum of the reactive species was simulated (Fig. 6b & Fig. S35), assuming the presence of two equivalent ^{27}Al nuclei, with the related hyperfine and quadrupole couplings of a_{iso} = 3.39 MHz, a_{dip} = [-0.88 0.03 0.86] MHz, P = -10.03 MHz (η = 0.185). These parameters are quite close to both ^{27}Al hyperfine and quadrupole tensors, estimated for the molecular precursor **1** (see ESI Section 3). This indicates that the Al atoms of the reactive species possess similar symmetry and coordinative surrounding as in **1**. The ^{1}H hyperfine coupling in $\mathbf{1_{500}}$-η-$\mathbf{a_{500}}$ was simulated to be a_{iso} = -0.5 ± 0.5 MHz, a_{dip} = [-4.75 ± 0.25; -4.75 ± 0.25; 9.5 ± 0.5] MHz, which corresponds to a Cu—H distance of 2.57 ± 0.05 Å within the point-dipole approximation. Such proton distance is attributed to the presence of hydroxyl group bound to the Cu(II) active sites.
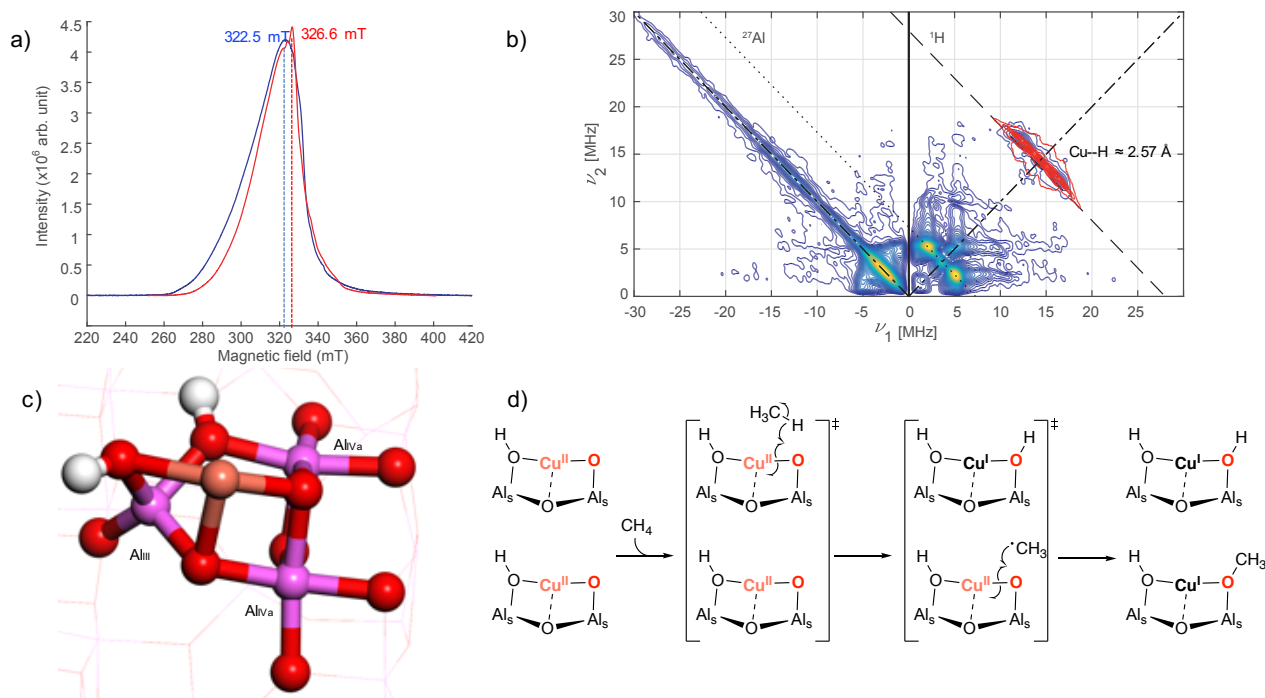
Figure 6. a) X-band echo detected spectra recorded at 10 K for supported catalysts before (**1$_{500}$-η-a$_{500}$**, red) and after reaction with CH$_4$ (**1$_{500}$-η-a$_{500}$ reacted**, blue). The dashed lines indicate the field position used to record the HYSCORE spectra. **b)** X-band HYSCORE spectrum of **1$_{500}$-γ-Al$_2$O$_{3-500}$** at 10 K recorded at the field of 326.6 mT, sum of three spectra with τ = [280 312 400] ns. Spectral intensity along the antidiagonal of (−+) quadrants is caused by phase cycling imperfection. Antidiagonal lines in the HYSCORE spectra indicate nuclear frequencies of ^{1}H (dashed) and ^{27}Al (dotted). The experimental spectrum is displayed in blue to yellow and the simulated ^{1}H ridge in red. **c)** DFT calculated structure of the reactive tricoordinated [(Al$_2$O)CuO(OH)]$^-$ site present on the (110) facet of γ-Al$_2$O$_3$. **d)** A possible 2 electron mechanism for CH$_4$ activation with 2 [(Al$_2$O)CuO(OH)]$^-$ through hydrogen abstraction followed reaction of the methyl radical.

The presence of a single, unique EPR signature for all reactive Cu(II) centers (site I) formed on different transition aluminas allows us to refine the geometrical configuration and surrounding environment of this center through combining the experimental evidences derived for the **1$_{500}$-γ-Al$_2$O$_{3-500}$** and **1$_{500}$-η-Al$_2$O$_{3-500}$** materials. The Cu(II) active sites have the following characteristics: i) they possess a coordinated hydroxyl group, ii) they are in close proximity to 2 equivalent Al$_{IV}$ sites, as shown for γ- and η-Al$_2$O$_3$ and iii) their formation is correlated to the presence of highly Lewis acidic Al$_{III}$ sites. Such features are strongly reminiscent of the structural characteristics of the (110) facet of γ-Al$_2$O$_3$,[37] or the related structures formed at the edge between the (110) and (100) facets.[38] We therefore explored possible structures for the active sites that would feature a characteristic, nearly-axial EPR signature, as well as reasonable formation energies. These Cu(II) species were modelled by adsorbing a CuO fragment onto various partially hydroxylated configurations of the (110) facet of γ-Al$_2$O$_3$ (1 H$_2$O per unit cell or 3 OH.nm^{-2} similar to the experimental OH density for γ-Al$_2$O$_{3-500}$ – 2.5 OH.nm^{-2} – see ESI section 8, Figs. S37-39). Among these, one model meets all aforementioned experimentally determined requirements (see also Fig. S38, model s1a_1). This model corresponds to a tri-coordinated Cu(II)-oxo site coordinated to two equivalent Al$_{IV}$ and an –OH bound to the so-called Al$_{III}$ with a Cu---H distance of 2.76 Å (Fig. 6c). The Cu---H distance is slightly longer than the experimental value (2.76 Å compared to 2.57 Å), likely a result of the shallow potential energy surface. In particular, the

9

T-shape geometry at Cu (Fig. 6c) is consistent with the EPR signature of the reactive species featuring a nearly axial g tensor.

Because the partial oxidation of CH_4 to CH_3OH is a two-electron process, two Cu(II) monomers must be involved since the Cu(II) sites are reduced to Cu(I) according to XANES and EPR spectroscopy. This process is feasible via an H-atom abstraction process on the hydroxyl or the oxo bound to Cu(II), generating an OH and a methyl radical that will generate a Cu(I) surface methoxy or CH_3OH species via a rebound mechanism involving the second Cu(II) site (Fig. 6d). Overall, this study shows that alumina is able to stabilize highly reactive isolated Cu(II) sites. EPR spectroscopy is shown here to be a particularly powerful characterization method, allowing the exclusive detection of the reactive monomeric sites involved in the partial oxidation of CH_4. The detection of a specific EPR signature for such active sites, which adopt a T-shape structure, is particularly noteworthy as it opens ways to tailor materials that can stabilize such type of structures. We are currently investigating alternative supports that could stabilize such species with the aim to increase the density of reactive sites.

References

1.   Lange, J. P., De Jong, K. P., Ansorge, J. & Tijm, P. J. A. Keys to methane conversion technologies. *Stud. Surf. Sci. Catal.* **107**, 81–86 (1997).

2.   Ahlquist, M., Nielsen, R. J., Periana, R. A. & Goddard, W. A. Product protection, the key to developing high performance methane selective oxidation catalysts. *J. Am. Chem. Soc.* **131**, 17110–17115 (2009).

3.   Ravi, M., Ranocchiari, M. & van Bokhoven, J. A. The Direct Catalytic Oxidation of Methane to Methanol—A Critical Assessment. *Angew. Chemie - Int. Ed.* **56**, 16464–16483 (2017).

4.   Latimer, A. A., Kakekhani, A., Kulkarni, A. R. & Nørskov, J. K. Direct Methane to Methanol: The Selectivity-Conversion Limit and Design Strategies. *ACS Catal.* **8**, 6894–6907 (2018).

5.   Lawton, T. J. & Rosenzweig, A. C. Methane-Oxidizing Enzymes: An Upstream Problem in Biological Gas-to-Liquids Conversion. *J. Am. Chem. Soc.* **138**, 9327–9340 (2016).

6.   Chan, S. I. *et al.* Redox potentiometry studies of particulate methane monooxygenase: Support for a trinuclear copper cluster active site. *Angew. Chemie - Int. Ed.* **46**, 1992–1994 (2007).

7.   Balasubramanian, R. *et al.* Oxidation of methane by a biological dicopper centre. *Nature* **465**, 115–119 (2010).

8.   Ross, M. O. *et al.* Particulate methane monooxygenase contains only mononuclear copper centers. *Science (80-.).* **364**, 566–570 (2019).

280 9. Lieberman, R. L. & Rosenzweig, A. C. Crystal structure of a membrane-bound metalloenzyme that catalyses the
281 biological oxidation of methane. *Nature* **434**, 177–182 (2005).

282 10. Starokon, E. V., Parfenov, M. V., Pirutko, L. V., Abornev, S. I. & Panov, G. I. Room-temperature oxidation of methane
283 by α-oxygen and extraction of products from the FeZSM-5 surface. *J. Phys. Chem. C* **115**, 2155–2161 (2011).

284 11. Groothaert, M. H., Smeets, P. J., Sels, B. F., Jacobs, P. A. & Schoonheydt, R. A. Selective oxidation of methane by the
285 bis(μ-oxo)dicopper core stabilized on ZSM-5 and mordenite zeolites. *J. Am. Chem. Soc.* **127**, 1394–1395 (2005).

286 12. Newton, M. A., Knorpp, A. J., Sushkevich, V. L., Palagin, D. & Van Bokhoven, J. A. Active sites and mechanisms in the
287 direct conversion of methane to methanol using Cu in zeolitic hosts: A critical examination. *Chem. Soc. Rev.* **49**, 1449–
288 1486 (2020).

289 13. Woertink, J. S. *et al.* A [Cu2O]2+ core in Cu-ZSM-5, the active site in the oxidation of methane to methanol. *Proc. Natl.*
290 *Acad. Sci. U. S. A.* **106**, 18908–18913 (2009).

291 14. Grundner, S. *et al.* Single-site trinuclear copper oxygen clusters in mordenite for selective conversion of methane to
292 methanol. *Nat. Commun.* **6**, 7546 (2015).

293 15. Kulkarni, A. R., Zhao, Z. J., Siahrostami, S., Nørskov, J. K. & Studt, F. Monocopper Active Site for Partial Methane
294 Oxidation in Cu-Exchanged 8MR Zeolites. *ACS Catal.* **6**, 6531–6536 (2016).

295 16. Sushkevich, V. L., Palagin, D. & van Bokhoven, J. A. The Effect of the Active-Site Structure on the Activity of Copper
296 Mordenite in the Aerobic and Anaerobic Conversion of Methane into Methanol. *Angew. Chemie - Int. Ed.* **57**, 8906–
297 8910 (2018).

298 17. Pappas, D. K. *et al.* The Nuclearity of the Active Site for Methane to Methanol Conversion in Cu-Mordenite: A
299 Quantitative Assessment. *J. Am. Chem. Soc.* **140**, 15270–15278 (2018).

300 18. Lange, J. P., Sushkevich, V. L., Knorpp, A. J. & Van Bokhoven, J. A. Methane-to-Methanol via Chemical Looping:
301 Economic Potential and Guidance for Future Research. *Ind. Eng. Chem. Res.* acs.iecr.9b01407 (2019).
302 doi:10.1021/acs.iecr.9b01407

303 19. Jovanovic, Z. R. *et al.* Oxidation of methane to methanol over Cu-exchanged zeolites: Scientia gratia scientiae or
304 paradigm shift in natural gas valorization? *J. Catal.* **385**, 238–245 (2020).

305 20. Le, H. V. *et al.* Stepwise Methane-to-Methanol Conversion on CuO/SBA-15. *Chem. - A Eur. J.* **24**, 12592–12599 (2018).

306 21. Bozbag, S. E. *et al.* Direct Stepwise Oxidation of Methane to Methanol over Cu-SiO2. *ACS Catal.* **8**, 5721–5731 (2018).

307 22. Wang, X. *et al.* Copper-modified zeolites and silica for conversion of methane to methanol. *Catalysts* **8**, 545 (2018).

308 23. Copéret, C. Fuels and energy carriers from single-site catalysts prepared via surface organometallic chemistry. *Nature*
309 *Energy* **4**, 1018–1024 (2019).

310 24. Meyet, J. *et al.* Monomeric Copper(II) Sites Supported on Alumina Selectively Convert Methane to Methanol. *Angew.*
311 *Chemie - Int. Ed.* **58**, 9841–9845 (2019).

312 25. Veith, M., Valtchev, K. & Huch, V. Tetraalkoxyaluminates of nickel(II), copper(II), and copper(I). *Inorg. Chem.* **47**, 1204–
313 1217 (2008).

314 26. Beebe, T. P., Crowell, J. E. & Yates, J. T. Infrared spectroscopic study of the rotation of chemisorbed methoxy species
315 on an alumina surface. *J. Chem. Phys.* **92**, 5119–5126 (1990).

316   27.   Comas Vives, A., Schwarzwälder, M., Copéret, C. & Sautet, P. Carbon carbon bond formation by activation of CH3F
317   on alumina. *J. Phys. Chem. C* **119**, 7156–7163 (2015).

318   28.   Newton, M. A. *et al.* On the Mechanism Underlying the Direct Conversion of Methane to Methanol by Copper Hosted
319   in Zeolites; Braiding Cu K-Edge XANES and Reactivity Studies. *J. Am. Chem. Soc.* **140**, 10090–10093 (2018).

320   29.   Busca, G. Structural, Surface, and Catalytic Properties of Aluminas. *Adv. Catal.* **57**, 319–404 (2014).

321   30.   Maciver, D. S., Tobin, H. H. & Barth, R. T. Catalytic aluminas I. Surface chemistry of eta and gamma alumina. *J. Catal.*
322   **2**, 485–497 (1963).

323   31.   Zubkov, S. A., Borovkov, V. Y., Gagarin, S. G. & Kazansky, V. B. Infrared study of nitrogen adsorption on alumina. *Chem.*
324   *Phys. Lett.* **107**, 337–340 (1984).

325   32.   Wischert, R., Copéret, C., Delbecq, F. & Sautet, P. Dinitrogen: A selective probe for tri-coordinate Al "defect" sites on
326   alumina. *Chem. Commun.* **47**, 4890–4892 (2011).

327   33.   Wischert, R., Laurent, P., Copéret, C., Delbecq, F. & Sautet, P. γ-Alumina: The Essential and Unexpected Role of Water
328   for the Structure, Stability, and Reactivity of "Defect" Sites. *J. Am. Chem. Soc.* **134**, 14430–14449 (2012).

329   34.   Szanyi, J. & Kwak, J. H. Dissecting the steps of CO2 reduction: 1. The interaction of CO and CO2 with γ-Al2O3: An in
330   situ FTIR study. *Phys. Chem. Chem. Phys.* **16**, 15117–15125 (2014).

331   35.   Gafurov, M. R. *et al.* Quantitative Analysis of Lewis Acid Centers of γ-Alumina by Using EPR of the Adsorbed
332   Anthraquinone as a Probe Molecule: Comparison with the Pyridine, Carbon Monoxide IR, and TPD of Ammonia. *J.*
333   *Phys. Chem. C* **119**, 27410–27415 (2015).

334   36.   Höfer, P., Grupp, A., Nebenführ, H. & Mehring, M. *Hyperfine sublevel correlation (hyscore) spectroscopy: a 2D ESR*
335   *investigation of the squaric acid radical. Chemical Physics Letters* **132**, (1986).

336   37.   Digne, M., Sautet, P., Raybaud, P., Euzen, P. & Toulhoat, H. Hydroxyl Groups on γ-Alumina Surfaces: A DFT Study. *J.*
337   *Catal.* **211**, 1–5 (2002).

338   38.   Batista, A. T. F. *et al.* Beyond γ-Al2O3 crystallite surfaces: The hidden features of edges revealed by solid-state 1H
339   NMR and DFT calculations. *J. Catal.* **378**, 140–143 (2019).

340